FINNED AIR-COOLING SYSTEM FOR LITHIUM-ION BATTERIES IN ELECTRIC VEHICLES

J. Luis Lopez-Osorio[a], *Ramon A. Soto-Ortega*[a], *Miguel S. Núñez-Aguayo*[a],
J. Luis Luviano-Ortiz[a] *and Abel Hernandez-Guerrero*[a*]

[a] *University of Guanajuato, Department of Mechanical Engineering, Salamanca, Mexico.*
**Corresponding author: abel@ugto.mx*

Abstract:

This paper presents a battery lithium-ion (LIB) cooling system for an electric vehicle, where efficiency and safety depend on the operating temperature of the batteries. Four different cooling schemes are proposed in this work and compared to a conventional design with airflow perpendicular to the batteries surface. A numerical analysis was carried out to compare three annular fins configurations (squared, triangular, and parabolic), a “manta ray-shaped” enclosure, with the conventional design. The results show that the conventional model reaches a maximum temperature of 333 K, while the geometry with square-profile annular fins exhibits a more uniform temperature distribution, reaching 314 K, with no evidence of vortices or recirculation. However, this greater heat dissipation requires higher pumping power, resulting in a higher friction factor than the other models. Conversely, the manta ray-shaped geometry has the lowest convective heat transfer coefficient but also exhibits the lowest friction factor and eliminates vorticities between (LIB), reflecting superior hydrodynamic performance and lower flow resistance.

Keywords:

Lithium-Ion Batteries, **Air Cooling System**, **Fins**, **Thermal Dissipation**, **Constructal Law**.

1. Introduction

The race toward sustainable transportation has made lithium-ion batteries (LIBs), the cornerstone of electric vehicles (EVs). For these batteries to effectively power EVs, they must first be kept below critical temperatures. The temperature of operation influences the electrochemical internal processes, affecting both the discharge capacity and the lifespan of the energy storage system, as it establishes a direct link with security and thermal conditions [1–3]. While the literature reports that the optimal operating temperature for LIBs is between 15 and 30 °C [1], Ali Alzwayi and Paul [4] report a broader range of 25 to 50 °C, depending on the application conditions.

Battery safety and degradation risks are critical outside of operating ranges. At temperatures above 40 °C, battery life decreases drastically. As He et al. [5] mention, each 1 °C increase reduces longevity by approximately two months, while, according to Alzwayi and Paul [4], the internal separator melts above 130 °C, causing short circuits. According to Almas’asfa et al. [6], when the battery’s operating temperature exceeds 200 °C, large amounts of heat are generated, potentially culminating in combustion or explosion. Experimental studies have shown that, without thermal management, batteries can reach temperatures above 50 °C at discharge rates of 2C and above 80 °C at 3C, far exceeding safe operating limits.

According to An et al. [3], at low temperatures, electrochemical kinetics deteriorate significantly, causing an increase in internal resistance and a reduction in discharge capacity. In contrast, He et al. [5] mention that extreme cold can freeze the electrolyte within the battery. The decomposition of metallic lithium generates slower ionic conductivity in the electrolyte at low temperatures, which has historically been considered the main reason for the poor performance of lithium-ion cells.

As the literature mentions, LIBs suffer at both temperature extremes [1, 2]. For this reason, Xie et al. [7] defines an operating window from -10 °C to 67 °C, depending on the ambient temperature and the discharge cycle. This proposal not only cools the cells but also ensures that the energy storage system remains within this safe operating window, maintaining its security and service life.

This intrinsic thermal peak occurs at low State of Charge (SOC) levels due to the interaction of specific electrical and thermodynamic parameters. According to research by Xie et al. [7], internal heat generation is primarily determined by the sum of irreversible heat, caused by ohmic (Ro) and polarization (Rp) resistances, and reversible heat, governed by the entropic heat coefficient (dU_{ocv}/dT). Experimental evidence indicates that as the battery reaches lower SOC levels, both types of resistance and the absolute value of the entropy coefficient increase significantly. This combination of factors results in massive heat production during the final stage of discharge.

Understanding the intrinsic thermal peak in lithium-ion batteries (LIBs) is essential for improving performance and ensuring safe operation. The advantages of air-cooling systems are manifold. Alzwayi et al. [4] cite their simple structure, low cost, and ease of implementation as the main attractions. However, Omar and Adham [8] argue that the decreased convective heat transfer coefficient of air is inadequate under high thermal loads.

Xu et al. [2] note that as air absorbs heat while passing through the battery pack, its cooling capacity progressively decreases towards the outlet, creating steep temperature gradients. In the context of this study, this aligns with the documented effects of thermal degradation: at 60 °C, the cycle life of lithium-ion batteries drops to 1,037 cycles compared to 3,323 cycles at 45 °C [1].

These limitations require more sophisticated thermal management approaches. He et al. [1] argues that air cooling is inadequate for high-speed, high-temperature conditions. As Omar and Adham [8] mention, integrating fins into cooling systems addresses the limitations of air cooling due to the increased surface area. The fins act as extended surfaces that improve the conductive path and facilitate better heat transfer [6].

The literature presents a variety of fin geometries for thermal cooling optimization [6]. Omar and Adham [8] mention spiral and circular fins. Additionally, Alma'asfa et al. [6] reports a significant reduction in temperature at high rates; however, this work needs to compare the results between the different models. Furthermore, [8] reports that spiral fins improve results compared to square fins. Parabolic profiles and "manta ray-shaped" fins produced results different from the conventional proposal.

The success of the fins is significantly related to the trajectories. Streamline optimization considers different parameters. For instance, non-square profiles can more effectively direct airflow along fin surfaces, thereby reducing flow separation and turbulence, which hinder heat transfer. Circular configurations demonstrate the effect of geometry on flow adhesion. Spiral structures optimize airflow toward battery surfaces, improving cooling efficiency while minimizing turbulence [4].

As discussed in this study, the "manta ray-shaped" shells leverage the hydrodynamic efficiency evolved in marine organisms to create flow channels that minimize turbulence and maximize the heat transfer contact area. The manta ray's aerodynamic shape evolved to minimize drag and maximize propulsive efficiency in fluid environments, suggesting the shells' potential applicability to engineered thermal management systems.

Any enhancement technique which affects heat transfer will also inevitably affect the friction factor or pumping power as well. This fact is caused by the increased skin friction in redeveloping the boundary layer and the occurrence of recirculation flow around the enhanced structures. If the height or number of fins per circle is increased, it would lead to an increased pressure drop.

Biomimetic design is not limited to casings. Various flow field adjustments for microchannel heat sinks (MCHs) have been investigated in literature to improve their thermal and hydraulic performance. [9]. These designs aim to surpass conventional linear or serpentine channel designs by altering the fluid path to increase heat transfer. Such designs can be seen in various environments, including leaves and stems. As Erick et al. [10] mention, this concept is part of the constructal law, which explains the universal phenomenon of designs generation and evolution, including the configuration, shape, structure, and pattern of all living things. The constructal law defines design evolution in physics, a concept closely linked to thermodynamics and has produced favorable results in heat distribution and transfer.

2. Methodology

2.1. Geometrical model

The cylindrical lithium-ion battery model NCR18650B by Panasonic was used. It has a diameter of 18 mm and a length of 65 mm, with a nominal voltage of 3.2 V and a capacity of 3.4 Ah. Twelve of these batteries were selected for designing the cooling system. In this study, three annular fin configurations, a "manta ray-shaped" enclosure, and a conventional branched cooling (CBC) system without fins were considered, as shown in Figure 1. The CBC system was based on the configuration proposed by Xie et al. [7], which does not consider constructal law branched ducts.

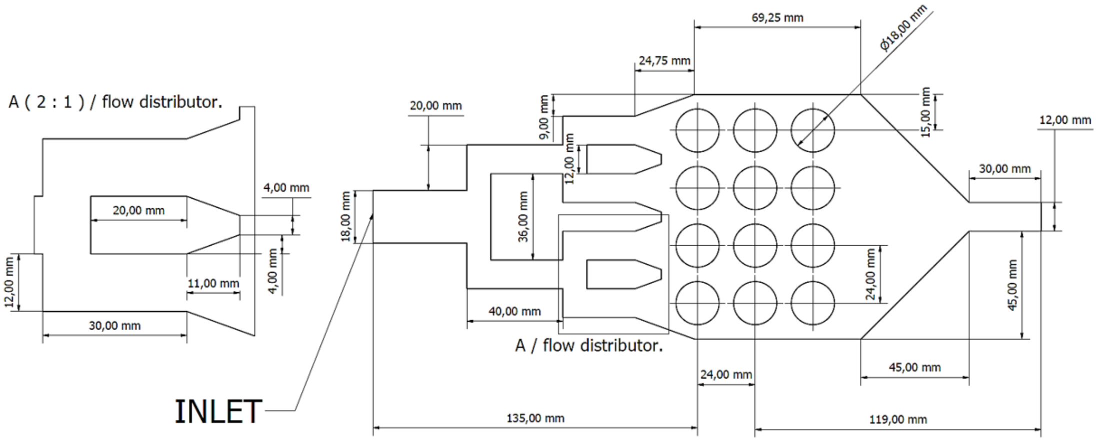

Figure 1: The conventional branched cooling design.

Additionally, a configuration with eight annular fins, each with a diameter of 20 mm and a different profile (triangular, square, or parabolic), was considered (Figure 2). Finally, the "manta ray-shaped" enclosure was applied to a row of lithium-ion batteries with an annular ring of 20 mm. The proposal includes two models.

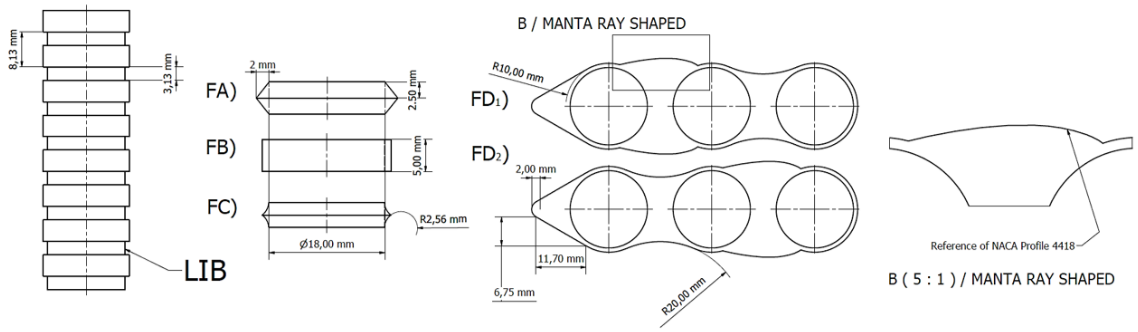

Figure 2: Full view of the draws FA) triangular, FB) square, FC) parabolic, FD_1) Manta ray-shaped one and FD_2) Manta ray-shaped two.

2.2. Boundary conditions

The simulations were conducted with a fluid inlet velocity of 3 m/s, corresponding to a Reynolds number (Re) of 5,773, indicating a turbulent regime. The inlet temperature was set to 300.15 K for all analyzed models. The most relevant boundary condition was the heat flux on the battery walls, set at 414.225 W/m^2. This heat flux value corresponds to the battery discharge rate. During experimentation with this phenomenon, the voltage remained constant, implying that the current was also constant.

These boundary conditions are directly governed by the volumetric heat generation rate q''', which characterizes the internal energy produced per unit volume of the cell. According to the electrothermal coupled model [7], q'' is determined by Equation (1):

$$q''' = \frac{1}{V_b}\left\{I^2\left[R_o + R_p\right] + IT\left(\frac{dU_{ocv}}{dT}\right)\right\} \tag{1}$$

Where V_b is the cell volume, I is the current, and R_o and R_p are the ohmic and polarization resistances, respectively. T is the cell temperature and dU_{ocv}/dT is the entropy coefficient. This internal generation establishes the thermal gradient that defines the heat flux across each battery face. The strategic arrangement of the annular fins facilitates dissipating the thermal load into the air-cooled environment.

The physical parameters, such as density and specific heat, were obtained using the lumped parameter method [9]. To accurately represent the mass of the component within the computational domain, the volumetric density ($\rho = 2932$ kg/m^3) was empirically determined from the manufacturer's mass and volume specifications (datasheet). The density of the internal assembly (jelly roll) was calculated using the rule of mixtures as shown in Equation (2):

$$\rho_{jr} = \sum(v_i \cdot \rho_i) \tag{2}$$

Since the thermal generation is concentrated in the internal active materials, the specific heat capacity $C_p = 988.5$ J/kg K) was derived by evaluating only the core assembly (jelly roll) analytically. This value was calculated using a mass-weighted average and the rule of mixtures, as shown in Equation (3), which incorporates the volume fractions of the electrodes, current collectors, and separators characteristic of the high-capacity NCA chemistry of this model:

$$C_{p,jr} = \frac{\sum(v_i \cdot \rho_i \cdot C_{p,i})}{\rho_{jr}} \tag{3}$$

Because of the layered structure of the cylindrical battery, the thermal conductivity coefficients in each direction can be obtained using the series and parallel resistance methods. The radial thermal conductivity (k_r) is determined by the series model, as shown in Equation (4), while the tangential and axial conductivities are calculated using the parallel model, as shown in Equation (5). Thus, the radial and axial / tangential thermal conductivities are 1.366 W/(m·K) and 18.118 W/(m·K),, respectively.

$$k_r = \frac{1}{\sum\left(\frac{v_i}{k_i}\right)} \tag{4}$$

$$k_z = \sum(v_i \cdot k_i) \tag{5}$$

The following considerations were made for the battery model to ensure an accurate solution:

1. A uniform heat flux on the battery pack.
2. Negligible convection and radiation losses within the battery.
3. The specific heat is constant and time independent.

4. The thermal properties of the fluid and the material are constant.

Figure 3 shows a schematic of the numerical model with the boundary conditions applied to all models. The parabolic profile annular fin configuration was used as the reference case. Aluminum was used for the fins, and air was used as the coolant. The thermophysical properties are summarized in Table 1.

Table 1: Thermophysical properties of the material and coolant.

Material	ρ [kg/m^3]	C$_p$ [J/kg K]	k [W/m K]	μ [kg/ms]
Air	1.177	1005	0.026	1.85×10^{-5}
Aluminum	2719	891	202.4	–

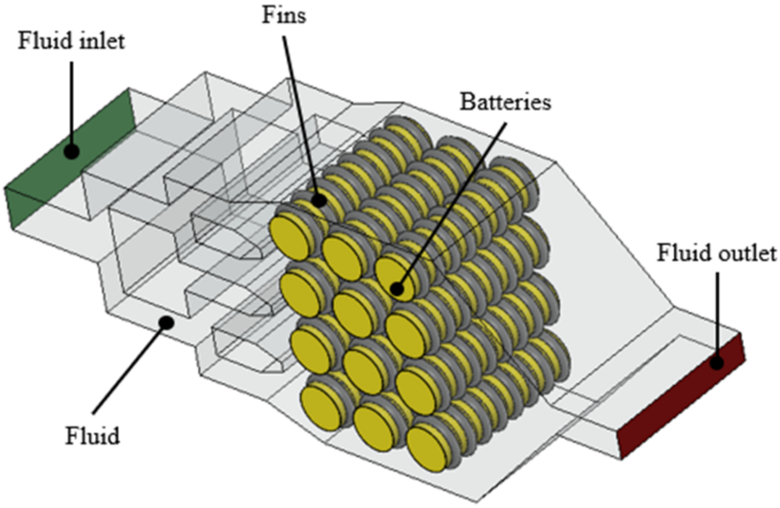

Figure 3: Boundary conditions of the model with parabolic-profile annular fins.

2.3. Governing equations

The governing equations for heat transfer phenomena in the fluid domain are the continuity equation and the energy and momentum conservation equations (Navier-Stokes equations). In the solid domain, the governing equation is the energy equation. These equations are discretized and solved using specialized finite volume software. Equation (6) is a simplified form of the continuity equation for the fluid domain.

$$\nabla \cdot \vec{V} = 0 \tag{6}$$

Equation (7) is a simplified momentum equation for each fluid direction:

$$\rho(\vec{V} \cdot \nabla)\vec{V} = -\nabla P + \mu \nabla^2 \vec{V} \tag{7}$$

Equations (8) and (9) are simplified energy equations for the fluid and solid domain, respectively

$$\rho C_p(\vec{V} \cdot \nabla T) = \kappa \nabla^2 T \tag{8}$$

$$\nabla \cdot (\kappa_s \nabla T_s) + \dot{q} = 0 \tag{9}$$

The κ-epsilon turbulence model is represented by Equations (10)–(12) [12]:

$$\nabla \cdot (\rho_m \vec{V}_m \kappa) = \nabla \cdot \left(\frac{\mu_{t,m}}{\sigma_\kappa} \nabla \kappa \right) + G_{\kappa,m} - \rho_m \varepsilon = 0 \tag{10}$$

$$\nabla \cdot (\rho_m \vec{D}_m \varepsilon) = \nabla \cdot \left(\frac{\mu_{t,m}}{\sigma_\varepsilon} \nabla \kappa \right) + (C_1 G_{\kappa,m} - C_2 \rho_m \varepsilon) = 0 \tag{11}$$

$$\mu_{t,m} = c_\mu \frac{\kappa^2}{\varepsilon} \rho_m, \qquad G_{\kappa,m} = \mu_{t,m} \left(\nabla \vec{V}_m + (\nabla \vec{V}_m)^T \right) \tag{12}$$

The parameters C_1, C_2, σ_k and σ_ε are turbulence model constants used to ensure simulation accuracy and stability. The values of these parameters are 1.44, 1.9, 1 and 1.2, respectively. They have been empirically determined and validated in numerous studies, making them highly accepted. They control the production and dissipation of turbulent kinetic energy, as well as the diffusion of the transport equations in the model [13].

The Nusselt number is given by the equation [14].

$$Nu = \frac{hD}{k} \tag{13}$$

Where D is the battery diameter, the thermal conductivity of the fluid was evaluated at the film temperature T_f. The global heat transfer coefficient, h, was determined by a simple energy balance:

$$h = \frac{q''}{N \Delta T_{ml}} \tag{14}$$

In Equation (15), N is total number of batteries, and ΔT_{ml} is the logarithmic mean temperature difference. The factor friction is given by:

$$f = \frac{\Delta P}{2} \frac{\rho}{V_{max}^2} \frac{D}{L} \tag{15}$$

The volumetric flow rate and the flow area are the same in both the enhanced model and the reference model. Therefore, the following expression is used to calculate effectiveness.

$$\eta = \frac{Nu/Nu_c}{f/f_c} \tag{16}$$

2.4. Numerical methods

ANSYS 2019 R3 Fluent, a commercial CFD software, was used to perform the 3D numerical simulation in this work. SolidWorks software was used to create the physical models prior to this stage. The finite volume method in Ansys was used to discretize the governing equations with a second-order upwind scheme. The unknown quantities at the cell faces were computed using a multidimensional linear reconstruction approach described in [15], which employs a Taylor series expansion of the cell-centered solution about the cell centroid to achieve higher-order accuracy at the cell faces. The SIMPLE algorithm of Patankar [16] was then chosen to solve the pressure-based equation derived from the momentum and mass continuity equations, coupling the velocity and pressure fields and solving them iteratively [9].

All these equations were solved sequentially and iteratively. The relaxation factors for pressure correction, density, momentum, and thermal energy were 0.3, 1, 0.7, and 1, respectively. Table 2 provides more detailed information on the solution methods and algorithms used.

The residuals for the continuity, momentum, energy, and k-ε model equations were set to a convergence value of 1×10^{-5}. For the energy equation, the residual was set to a convergence value of 1×10^{-6}.

Table 2: Characteristics of the numerical model.

Solver	
Type	Pressure-based
Velocity formulation	Absolute
Time	Steady
Model	
Viscosity	$k-\varepsilon$ **turbulence model**
Solution methods	
Pressure-velocity coupling	SIMPLE scheme
Spatial discretization	
Continuity equation	Second Order
Momentum equation	
Energy	
Turbulent kinetic energy	First Order
Turbulent disipation rate	

2.5. Model verification

To validate the numerical simulation of the cooling system, it was compared with the experimental data of Xie et al. [7], who conducted testing with a battery cell discharge of 1 C with a constant current and 0.4 state of charge (SOC). The surrounding temperature during the experiments was 27 °C. The relative error was less than 2% for each battery, indicating that the simulation agrees well with the experimental data. The relative error between the simulated and experimental values of the average wall temperature of the battery is presented in Figure 4.

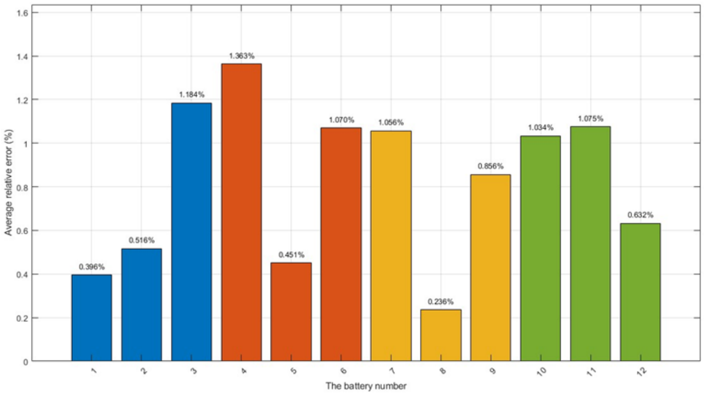

Figure 4: Average relative error at a 1 C discharge rate and 27°C ambient temperature.

2.6. Grid independence test

An individuality test was performed on the mesh to evaluate the accuracy and consistency of the numerical solutions for a battery pack. In this study, the conventional configuration was chosen, and eight different mesh models were analyzed, containing 115,272; 115,613; 118,063; 118,878; 120,880; 123,793; 129,517; and 142,266 elements, respectively. The analysis focused on the average wall temperature of the batteries. The numerical results showed that this parameter stabilized with a mesh size of 129,517, with a deviation of less than 0.035% for $\Delta T_{\max}$. Given this stability, a mesh with 142,266 elements was selected for further simulations, achieving a balance between computational efficiency and the accuracy of the results.

3. Results

3.1. Temperature contours

Figure 5(a) shows the conventional model, which has a non-uniform temperature distribution. The fluid temperature is higher in the first rows, and a heat stagnation zone is identified in the upper row, increasing the temperature of the batteries in this region to 318.5 K. The temperature contour of the model with square-profile annular fins indicates that the right-side rows do not exhibit improved heat distribution compared to the adjacent rows, reaching a temperature of 312 K (Figure 5(b)). Figure 5(c) shows that the model with triangular-profile annular fins improves the temperature distribution; however, an increase in temperature can be observed in the last columns.

A more pronounced heat stagnation zone is observed in the model with parabolic-profile annular fins compared to the conventional model. However, the thermal contour along the fins indicates a more pronounced temperature gradient than in the previously mentioned models. The batteries in the last row exhibit enhanced heat transfer, reaching a temperature of 311 K. Figure 5(e) shows the "manta ray-shaped" enclosure model, where the central columns do not provide effective heat dissipation, resulting in a maximum temperature of 315 K, which is higher than that of the models with square, triangular, or parabolic annular fins.

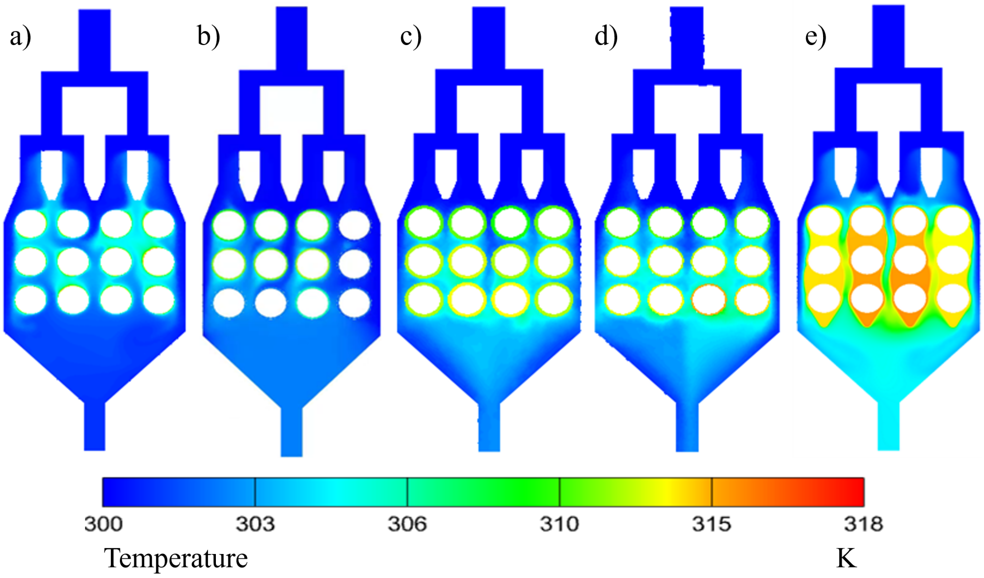

Figure 5: Temperature contour of the models: (a) conventional model, annular fin model with (b) square, (c) triangular, and (d) parabolic profiles, and (e) manta-ray shaped enclosure.

3.2. Streamlines

Figure 6 shows non-uniform flow behavior in all models, as fluid particles tend to follow paths of least resistance, forming preferential channels with an average velocity of 1 m/s. Figure 6(a) shows vortices generating low-velocity regions between the batteries. Figures 6(b) and 6(c) show that models with annular fins of square and triangular profiles, respectively, largely eliminate recirculation zones and increase the effective contact area between the batteries and the fluid. In Figure 6(b), the fluid velocity is higher than in the other models, reaching 2.5 m/s, due to the square profile of the fins accelerating the air particles. Figure 6(d), corresponding to the parabolic profile, shows a reduction in coherent eddy structures but still presents multiple low-velocity regions. The "manta ray-shaped" enclosure model (Figure 6(e)) eliminates stagnation zones, improving flow distribution.

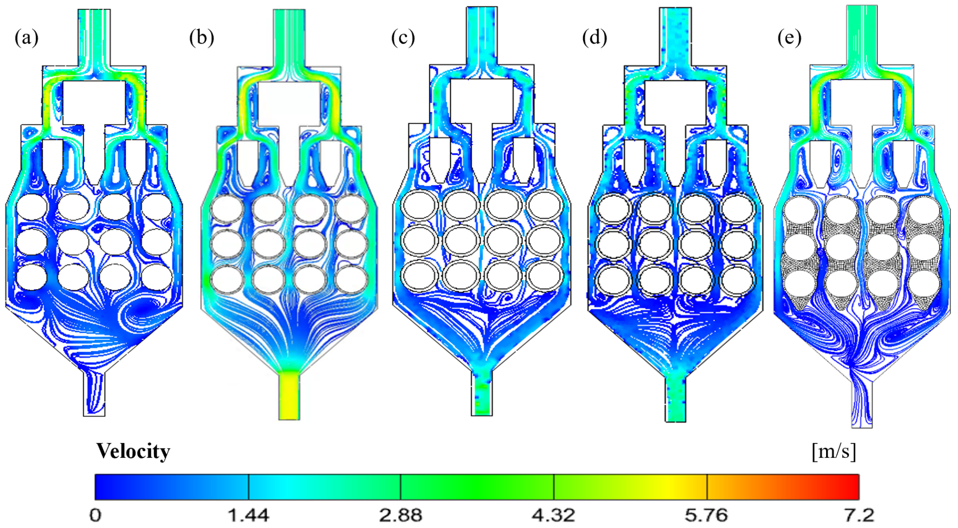

Figure 6: Streamlines of the models: (a) conventional model, (b) annular fins with square profile, (c) annular fins with triangular profile, (d) annular fins with parabolic profile, and (e) manta-ray shaped enclosure.

3.3. Friction factor and convective coefficient

Figure 7 presents a comparative analysis of the thermohydrodynamic performance of the evaluated models. Figure 7(a) shows the friction factor, allowing a direct comparison of the pressure drop across configurations. Figure 7(b) displays the convective heat transfer coefficient, providing insight into the thermal efficiency of each cooling system. The model with annular square fins exhibits the highest convective coefficient, indicating enhanced heat dissipation capability. However, this improvement is accompanied by an increased friction factor, implying a higher pumping power requirement. In contrast, the conventional model and the model with annular parabolic fins show lower convective coefficients and reduced friction factors. This behavior is associated with the formation of recirculation zones between the batteries, which limit fluid mixing and decrease heat transfer effectiveness by reducing temperature gradients between the coolant and battery surfaces.

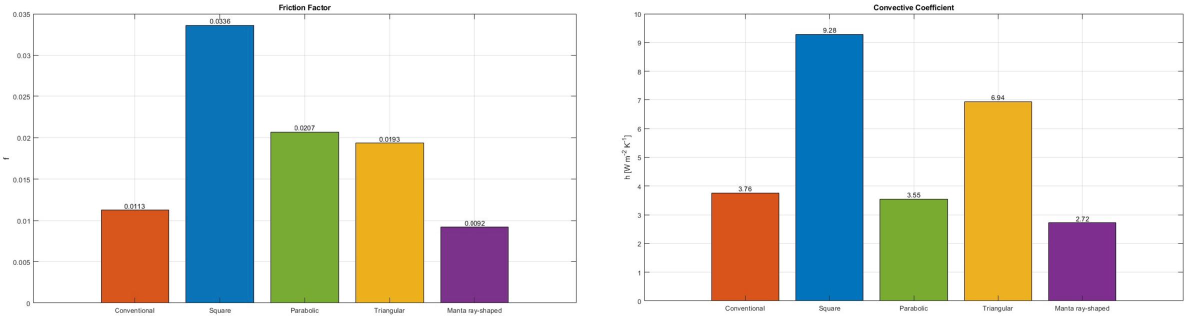

a) b)

Figure 7: Graph of the convective coefficient in each of the models.

3.4. Effectiveness

Finally, Figure 8 shows the effectiveness calculated for each model relative to the conventional model. For most cases, effectiveness remains below unity, indicating that the increase in friction outweighs the enhancement in heat dissipation. However, the model with annular fins of triangular profile reaches an effectiveness close to unity, indicating no net improvement in energy efficiency. Additionally, for the model with annular fins parabolic profile, the relative friction exceeds the heat transfer by approximately a factor of two, mainly due to the roughness and corrugation associated with the fin geometry.

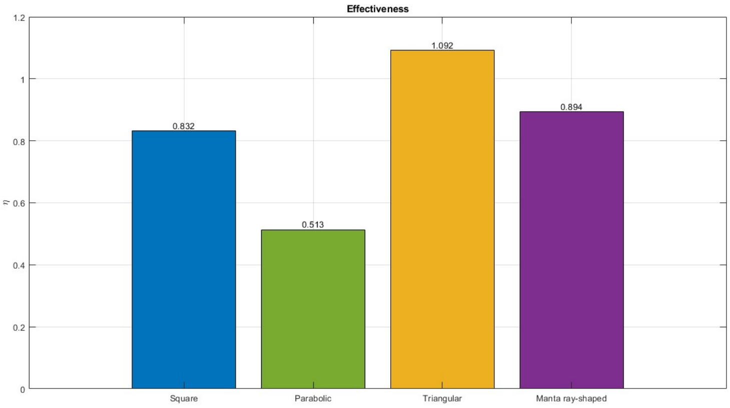

Figure 8: Graph of the effectiveness in each of the models.

4. Conclusions

The proposed cooling system for LIBs produced significantly better thermal performance than the conventional design, maintaining battery temperatures within the optimal operating window defined in the introduction even under demanding conditions. This was true even when the state of charge (SOC) reached 0.4 and the operation was abrupt. The square and triangular annular fin geometries achieved a more uniform temperature distribution, largely eliminating flow recirculation zones and increasing the thermal contact area. This improvement in flow uniformity directly contributes to reducing hotspots, which are critical for extending battery life, preventing thermal runaway events, and ensuring safe operation at high discharge rates. The square profile notably accelerates airflow to velocities exceeding 2.5 m/s, exhibiting the highest convective coefficient and indicating optimal heat dissipation. In addition, integrating nature-inspired designs, such as the manta ray-shaped casing and constructal-based distributors based on constructal principles, provided fundamental improvements in thermal management. The biomimetic casing leverages hydrodynamic efficiency to create flow channels that minimize turbulence and aerodynamic drag while maximizing the contact area for heat transfer. This approach demonstrates the potential of biomimetic and constructal designs to achieve passive thermal control, reducing reliance on energy-intensive active cooling systems. Applying constructal design principles yielded highly favorable results in the even distribution of air and heat, overcoming the limitations of conventional systems where cooling capacity progressively decreases towards the outlet. Furthermore, these designs promote energy efficiency by reducing pressure losses, thereby lowering the fan power requirements in real-world EV applications.

Overall, these configuration strategies provide an effective solution to the thermal loads inherent in the discharge cycle, achieving efficient passive cooling without the use of active mechanisms or additional energy input. While conventional models that employ fins exhibited lower convective coefficients due to recirculation zones, models like the Manta Ray design eliminate this circulation between the batteries by guiding airflow more efficiently. These proposals ultimately ensure that energy storage operates within a safe thermal window, guaranteeing the efficiency, safety, and lifespan of electric vehicles.

Nomenclature

Letter symbols

A	flow area, m^2
C_1	turbulence model constant
C_2	turbulence model constant
C_p	specific heat capacity, $\mathrm{J/(kg \cdot K)}$
D	battery diameter, m

dU_{ocv}/dT	entropy coefficient, $\mathrm{V/K}$
f	friction factor
h	convective heat transfer coefficient, $\mathrm{W/(m^2 \cdot K)}$
I	electric current, A
k	thermal conductivity, $\mathrm{W/(m \cdot K)}$
L	characteristic length, m
N	number of batteries
Nu	Nusselt number
P	pressure, Pa
q''	heat flux, $\mathrm{W/m^2}$
q'''	volumetric heat generation rate, $\mathrm{W/m^3}$
R_o	ohmic resistance, Ω
R_p	polarization resistance, Ω
Re	Reynolds number
T	temperature, K
V	velocity, $\mathrm{m/s}$
V_b	battery volume, $\mathrm{m^3}$
V_{max}	maximum velocity, $\mathrm{m/s}$
v_i	volume fraction
ΔP	pressure drop, Pa
ΔT_{ml}	logarithmic mean temperature difference, K

Greek symbols

ϵ	turbulent dissipation rate
η	thermal-hydraulic effectiveness
κ	turbulent kinetic energy
μ	dynamic viscosity, $\mathrm{kg/(m \cdot s)}$
μ_t	turbulent viscosity
ρ	density, $\mathrm{kg/m^3}$
σ_k	turbulent Prandtl number for κ
σ_ϵ	turbulent Prandtl number for ϵ

Subscripts and superscripts

b	battery
c	conventional model
f	fluid / film
i	component
jr	jelly roll
max	maximum value
o	ohmic
p	polarization
r	radial direction
s	solid
z	axial direction

References

[1] Kim J., Oh J., Lee H. *Review on battery thermal management system for electric vehicles*. Applied Thermal Engineering 2019;149:192-212.

[2] Xu H., Zhang X., Xiang G., Li H. *Optimization of liquid cooling and heat dissipation system of lithium-ion battery packs of automobile*. Case Studies in Thermal Engineering 2021;26:101012.

[3] An Z., Jia L., Wei L., Dang C., Peng Q. *Investigation on lithium-ion battery electrochemical and thermal characteristic based on electrochemical-thermal coupled model*. Applied Thermal Engineering 2018;137:792-807.

[4] Alzwayi A., Paul M.C. *Enhancing battery cooling and temperature uniformity with longitudinal airflow and fin configurations*. Applied Thermal Engineering 2025;265:125625.

[5] He L., Gu Z., Zhang Y., Jing H., Li P. *Review on Thermal Management of Lithium-Ion Batteries for Electric Vehicles: Advances, Challenges, and Outlook*. Energy & Fuels 2023;37(7):4835-57.

[6] Alma'asfa S.I., Abdul Aziz M.S., Khor C.Y., Fraige F.Y. *Thermal management of cylindrical lithium-ion batteries with different fin configurations and phase change material: a numerical analysis*. Journal of Thermal Analysis and Calorimetry 2025;150(16):12643-62.

[7] Xie Y., Wang X., Li W., Zhang Y., Dan D., Li K., Feng F., Wu C., Wang P. *A resistance-based electro-thermal coupled model for an air-cooled battery pack that considers branch current variation*. International Journal of Thermal Sciences 2021;159:106611.

[8] Omar A.A., Adham A.M. *Thermal analysis of lithium-ion batteries using forced-air cooling and circular fin systems: A numerical study*. International Journal of Thermofluids 2025;27:101212.

[9] Imran A.A., Mahmoud N.S., Jaffal H.M. *Numerical and experimental investigation of heat transfer in liquid cooling serpentine mini-channel heat sink with different new configuration models*. Thermal Science and Engineering Progress 2018;6:128-39.

[10] Nava-Arriaga E.M., Hernandez-Guerrero A., Luviano-Ortiz J.L., Bejan A. *Heat sinks with minichannels and flow distributors based on constructal law*. International Communications in Heat and Mass Transfer 2021;125:105122.

[11] Baazouzi S., Feistel N., Wanner J., Landwehr I., Fill A., Birke K.P. *Design, Properties, and Manufacturing of Cylindrical Li-Ion Battery Cells—A Generic Overview*. Batteries 2023;9(6):309.

[12] Bazdar H., Toghraie D., Pourfattah F., Akbari O.A., Nguyen H.M., Asadi A. *Numerical investigation of turbulent flow and heat transfer of nanofluid inside a wavy microchannel with different wavelengths*. Journal of Thermal Analysis and Calorimetry 2020;139(3):2365-80.

[13] Fezoui L., Stoufflet B. *A class of implicit upwind schemes for Euler simulations with unstructured meshes*. J. Comput. Phys. 1989;84(1):174-206.

[14] Ji W.-T., Fan J.-F., Zhao C.-Y., Tao W.-Q. *A revised performance evaluation method for energy saving effectiveness of heat transfer enhancement techniques*. International Journal of Heat and Mass Transfer 2019;138:1142-1153.

[15] Khalil M., Hassan Ali M.I., Khan K.A., Abu Al-Rub R. *Forced convection heat transfer in heat sinks with topologies based on triply periodic minimal surfaces*. Case Studies in Thermal Engineering 2022;38:102313.

[16] Patankar S. *Numerical Heat Transfer and Fluid Flow*. New York: Hemisphere Publishing; 1980.